Energy Storage

WILEY

ENERGY STORAGE

RESEARCH ARTICLE OPEN ACCESS

Corrosion of Stellite Alloys and WC-Based Cemented Ceramics Exposed to Oxygen-Containing Molten Pb at 600°C and 700°C

Anisa Purwitasari | Renate Fetzer | Annette Heinzel | Alfons Weisenburger | Georg Müller

Institute for Pulsed Power and Microwave Technology (IHM), Karlsruhe Institute of Technology (KIT), Karlsruhe, Germany

Correspondence: Renate Fetzer (renate.fetzer@kit.edu)

Received: 22 August 2025 | **Revised:** 8 January 2026 | **Accepted:** 12 January 2026

Keywords: co-based alloys | corrosion | dissolution | liquid lead | oxidation | tungsten carbide

ABSTRACT

Liquid metals such as molten lead (Pb) are attractive heat transfer fluids for high-temperature thermal energy storage systems. Although extensive research is performed on the corrosion behavior of structural steels and Fe-based alloys in liquid Pb, the corrosion resistance of materials with high wear resistance in such environments is less explored. In order to expand the knowledge on the compatibility of wear-resistant materials with molten Pb in a temperature range relevant for high-temperature thermal energy storage systems, the current study investigates for the first time Pb corrosion of the two commercial Co-Cr-based alloys Stellite 21 and Stellite 6 and of two commercial tungsten carbide (WC) ceramics, one with Co binder and the other with Ni/Cr binder, in the temperature range from 600°C to 700°C. Static exposure tests in molten Pb containing 2×10^{-7} wt.% dissolved oxygen are performed for up to 5000 h. The results reveal the formation of Cr-rich oxides on the surfaces of all materials, though an oxide scale with protective properties is found for Stellite 6 at 700°C only. Here, the scale is composed of an outer Cr-rich oxide layer and an inner Si-rich oxide. In all other cases, dissolution of alloying elements (Co-Cr-based alloys) and of the binder phase (WC-based ceramics) is observed to various extents, which gives first indications for the service life of respective components exposed to liquid Pb environments.

1 | Introduction

High-temperature thermal energy storage (TES) systems are under development worldwide due to the growing integration of renewable energy sources and the possibility to store waste heat from industrial processes for reuse or for other processes [1, 2]. As the temperature increases, the choice of heat transport fluids (HTFs) becomes more challenging. Conventional HTFs like thermal oil and nitrate salt decompose at approximately 400°C and 565°C, respectively [3, 4]. At higher temperatures, gases like air, CO_2, and helium, high-melting molten salts like chlorides, or liquid metals can be used. The latter in particular are characterized by an excellent thermal conductivity [5]. Liquid metals under consideration as HTF are alkali metals such as sodium [6–8] or heavy metals [3, 9]. In contrast to sodium, which is highly reactive and the use of which involves the risks of fire and explosion, heavy liquid metals offer high safety at the expense of a higher corrosion rate. The feasibility of heavy liquid metals used as HTF in packed-bed TES systems has been demonstrated numerically [10] and experimentally [11]. Regarding the corrosivity and material compatibility, liquid tin shows one of the most aggressive corrosion behaviors among the heavy liquid metals under consideration for high-temperature TES systems, including strong dissolution of alloying elements such as Ni, Fe, and Cr, and formation of intermetallic phases [12, 13]. Liquid lead (Pb) and lead-bismuth eutectic (LBE) show lower corrosion rates due to their lower solubility of alloying elements and their inability to form intermetallic phases [3, 9, 14]. Compared with LBE, pure Pb is cheaper and is slightly less corrosive due to

its lower solubility of alloying elements, which offers advantages for high-temperature applications where alloying with the lower melting bismuth is not required.

Motivated by the use of Pb or LBE as HTF in advanced nuclear energy applications (lead-cooled fast reactors), extensive studies have investigated the corrosion behavior of structural materials, particularly of ferritic/martensitic or austenitic steels, in liquid Pb and LBE across a wide range of dissolved oxygen concentrations and temperatures [15–23]. These studies revealed the primary corrosion mechanisms including selective dissolution of alloying elements, oxidation, and liquid metal penetration. Dissolved oxygen in the liquid Pb or LBE is employed to enable an in situ growth of a protective oxide layer on the steel surface, which serves as a barrier against the liquid metal attack. Typically, an oxygen content between 10^{-7} and 10^{-6} wt.% is used, which allows iron oxides to grow over a wide temperature range without the formation of Pb oxide [24]. With 2×10^{-7} wt.% oxygen dissolved in liquid Pb, acceptable corrosion resistance could be shown for commercial austenitic and ferritic-martensitic steels for temperatures up to 700°C [25, 26], while surface-aluminizing further improves the corrosion resistance at these exposure conditions [26, 27]. Liquid Pb or LBE corrosion is particularly pronounced in components that are simultaneously exposed to mechanical wear or tribological stresses. Examples are fuel cladding or heat exchanger tubes, where the interaction between corrosion and wear can lead to accelerated material failure [28, 29].

Components that experience high mechanical loads such as pumps or valves require materials with high wear resistance. Due to the low wear resistance of conventional structural steels, surface hardening treatments such as hard facing are commonly employed to enhance their performance under tribological conditions [30–33]. These treatments typically involve the application of wear-resistant materials such as cobalt (Co)- or nickel (Ni)-based alloys onto the base metals. Due to the high solubility and preferential dissolution of nickel, Ni-based alloys have demonstrated limited compatibility with molten Pb and LBE [34, 35]. Accordingly, Ni-based alloys are not regarded as potential candidates for applications in liquid Pb. The solubility of Co in Pb is significantly lower than that of Ni and only slightly higher than the solubility of Fe [36, 37]. However, similar to Ni and in contrast to Fe, the above-mentioned oxygen concentrations do not allow oxidation of Co. The formation of a protective oxide scale on Co-based alloys therefore depends on the other alloying elements. Here Co–Cr-based alloys such as Stellite alloys are promising candidates for high-temperature TES systems, since Cr is known as a strong oxide former capable of forming a protective oxide scale. Because Co is excluded from use in nuclear applications due to its high activation, the compatibility of Co-based alloys with liquid Pb is still little explored, and no study is available yet on the Pb corrosion of Stellite alloys.

An alternative to hard facing is the use of wear-resistant bulk materials, e.g., ceramics, for components with high mechanical loads. Regarding the compatibility of ceramic materials with liquid Pb or LBE, the study by Takahashi and Kondo highlighted the excellent compatibility of Si_3N_4 and SiC when exposed to flowing liquid lead-bismuth eutectic at temperatures around 550°C and an oxygen concentration of 10^{-6} wt.% [38]. Their observation indicated that the weight loss of these ceramic materials was significantly lower compared to that of steels, suggesting their potential as more corrosion-resistant materials. Following these promising results, further studies on the corrosion behavior of SiC in LBE environments have been performed [39, 40]. However, no study is available yet on the use of WC-based ceramics in a liquid Pb environment.

The current study investigates the material compatibility with liquid Pb for several commercially available materials with high wear resistance that have not been studied before. Two Co-Cr-based alloys, Stellite 21 and Stellite 6, as well as tungsten carbide (WC) with two different binder elements (Co and Ni/Cr) are selected. To explore their potential use in high-temperature TES systems with Pb as HTF, corrosion tests are performed for up to 5000 h at two different temperatures, 600°C and 700°C, and at a target oxygen concentration of 2×10^{-7} wt.%.

2 | Materials and Methods

2.1 | Materials

Two Co-Cr-based alloys, Stellite 21 and Stellite 6, were selected for the exposure tests. Both alloys were supplied by KSB SE & Co. KGaA as rods with 4 mm diameter. The chemical compositions of the metal alloys, as specified in the material charge certificates, are summarized in Table 1. The main differences in composition are the deviating C contents and the presence of Mo (Stellite 21) and W (Stellite 6), respectively, while Cr and Ni contents are similar for both materials. In addition to the metal alloys, two ceramic materials were included in the test program: tungsten carbide with Co binder (WC–Co) and tungsten carbide with Ni/Cr binder (WC–Ni–Cr). The WC-based cemented carbides were provided by Kennametal Inc. The WC–Co cemented ceramic contained 10.0% Co binder, 89.3% WC, and 0.7% other carbides, while WC–Ni–Cr contained 9.2% Ni/Cr binder, 90.3% WC, and 0.5% other carbides. Lead (Pb) with a purity of 99.995% was used for the corrosion tests, supplied in bar form by HMW Hauner GmbH & Co. KG.

2.2 | Corrosion Tests

The exposure tests were performed in the COSTA facility, which allows simultaneous control of the exposure temperature and

TABLE 1 | Chemical composition of Co–Cr-based alloys in wt.%.

Material	Co	C	Mn	Cr	Ni	Si	Fe	Mo	W
Stellite 21	Bal.	0.3	0.12	28	2.5	0.8	2.0	5.0	—
Stellite 6	Bal.	1.03	0.5	28.76	2.34	0.56	3.8	—	5.06

the oxygen content of the liquid Pb [41]. The Pb was melted and subsequently cast into alumina crucibles. The Pb-filled alumina crucibles were then placed inside a quartz glass tube located in a tubular furnace. The gas atmosphere in the glass tube was controlled by a continuous flow of a gas mixture with defined H_2/H_2O ratio, which determined the concentration of oxygen dissolved in the liquid Pb (target oxygen concentration 2×10^{-7} wt.%). After reaching equilibrium between the oxygen activity in the gas phase and the dissolved oxygen in the molten Pb at the given test temperature (600°C and 700°C, respectively), the test samples were introduced via a conditioned glovebox to avoid excessive oxygen ingress. Each crucible was loaded with one specimen, with the ratio of exposed surface area to liquid Pb volume below 270 cm^2/L. During the exposure tests, the oxygen content was continuously monitored. Values between 1×10^{-7} and 2×10^{-7} wt.% were obtained for the tests at 600°C, while slightly higher values between 1×10^{-7} and 5×10^{-7} wt.% existed during the 700°C tests. When reaching the end of the exposure tests, the conditioned glovebox was once more employed for unloading the samples. Table 2 summarizes the tested materials and the respective exposure times.

2.3 | Characterization Methods

After removal from the COSTA facility, each sample was cut into two parts, with one part used for cross-sectional analysis. To preserve the corrosion products, no cleaning was performed prior to embedding the samples in resin. Stellite samples were ground using silicon carbide paper up to 2400 grit, while ceramic samples were prepared with abrasive grinding disks and polished using a diamond suspension. Cross-sectional analysis was carried out using scanning electron microscopy (SEM, Zeiss LEO 1530 VP) coupled with energy-dispersive X-ray spectroscopy (EDS). The specimens were analyzed at many different locations, which gives confidence in the statistical variation of the results. When additional surface or oxide crystal structure analysis by X-ray diffraction (XRD, Seifert 3003 PTS) was required, the second part of the sample was cleaned beforehand using a 1:1:1 solution of acetic acid (CH_3COOH), hydrogen peroxide, and ethanol.

3 | Results and Discussion

3.1 | Stellite 21

Figure 1a presents an image of the Stellite 21 sample after 2000 h of exposure at 600°C in liquid Pb at low magnification. Notably, penetration of the liquid Pb can be observed across the entire sample surface to a maximum depth of 40 μm. The higher-magnification image shown in Figure 1b, along with the corresponding EDS elemental mapping presented in Figure 1d, provides clear evidence of ongoing dissolution corrosion occurring near the sample surface, which results in the formation of rather large voids in the corroded region (Figure 1b). The voids are only partially filled with Pb, which indicates that outward diffusion of Stellite 21 alloying elements (mainly Cr) proceeds much faster than the penetration of Pb. The described corrosion behavior is observed in the presence of a continuous Cr-rich oxide scale (see elevated O and Cr signals along the sample surface in the EDS elemental mapping images in Figure 1d), showing that the oxide layer is not protective. Responsible for the non-protective properties could be small defects or an insufficient density and compactness of the scale. Although the oxide scale is not protective, it acts as a diffusion barrier and slows down the dissolution and Pb penetration. As further seen in Figure 1d (signals of Cr and Co), the corroded region exhibits significant Cr depletion in addition to the void formation, accompanied by enrichment of Co in the remaining material. This compositional change is attributed to the selective oxidation of Cr as well as the selective dissolution of Cr into the liquid Pb. Regarding the minor alloying elements of Stellite 21, a slight depletion in Ni is observed in the corrosion-affected region due to Ni dissolution (Ni signal in Figure 1d). Si, Fe, and Mo seem not to play any significant role in the corrosion/oxidation behavior of Stellite 21 at 600°C.

As shown in Figure 1c, the Stellite 21 alloy exhibits a comparable corrosion behavior after exposure at 700°C, with formation of a non-protective Cr-rich oxide scale, selective dissolution and void formation, and Pb penetration to similar depths. Compared with the exposure at 600°C, much fewer and larger voids are formed at 700°C. Additionally, the oxide scale is found to be enriched in Si at the boundary to the bulk material. The differences in corrosion behavior are attributed to microstructural changes of Stellite 21 at 700°C, see inset to Figure 1c compared with inset to Figure 1a.

Regarding the corrosion rate, Stellite 21 is corroded at both temperatures to a depth of around 40 μm after 2000 h of exposure, which corresponds to 0.18 mm per year if assuming a linear corrosion behavior.

TABLE 2 | Materials and exposure times of corrosion tests in liquid Pb containing 2×10^{-7} wt.% dissolved oxygen.

Material	600°C	700°C
Stellite 21	2000 h	2000 h
Stellite 6	5000 h	5000 h
WC–Co	5000 h	—
WC–Ni–Cr	2000 h	2000 h, 5000 h

3.2 | Stellite 6

Figure 2a shows a cross-sectional image of Stellite 6 after 5000 h of exposure in liquid Pb at 600°C. Corrosion attacks and liquid Pb penetration are clearly evident to a maximum depth of approximately 200 μm. Assuming a constant corrosion rate, this corresponds to a corrosion depth of 0.35 mm after 1 year. Based on the higher-magnification image and EDS elemental mapping presented in Figure 2b,c, dissolution corrosion is observed, leaving behind a rather porous structure (see right side of the imaged region). As revealed by the EDS elemental mappings in Figure 2c, the porous structure is composed of an inward-growing Cr-rich oxide, a Cr-depleted and Co–Fe-enriched region below the oxide, and Si–W-rich remains above the oxide. Pb is found entrained above the oxide and penetrated into the voids below the oxide, next to the bulk material. These results indicate that Cr was not able to oxidize to a continuous, stable, and

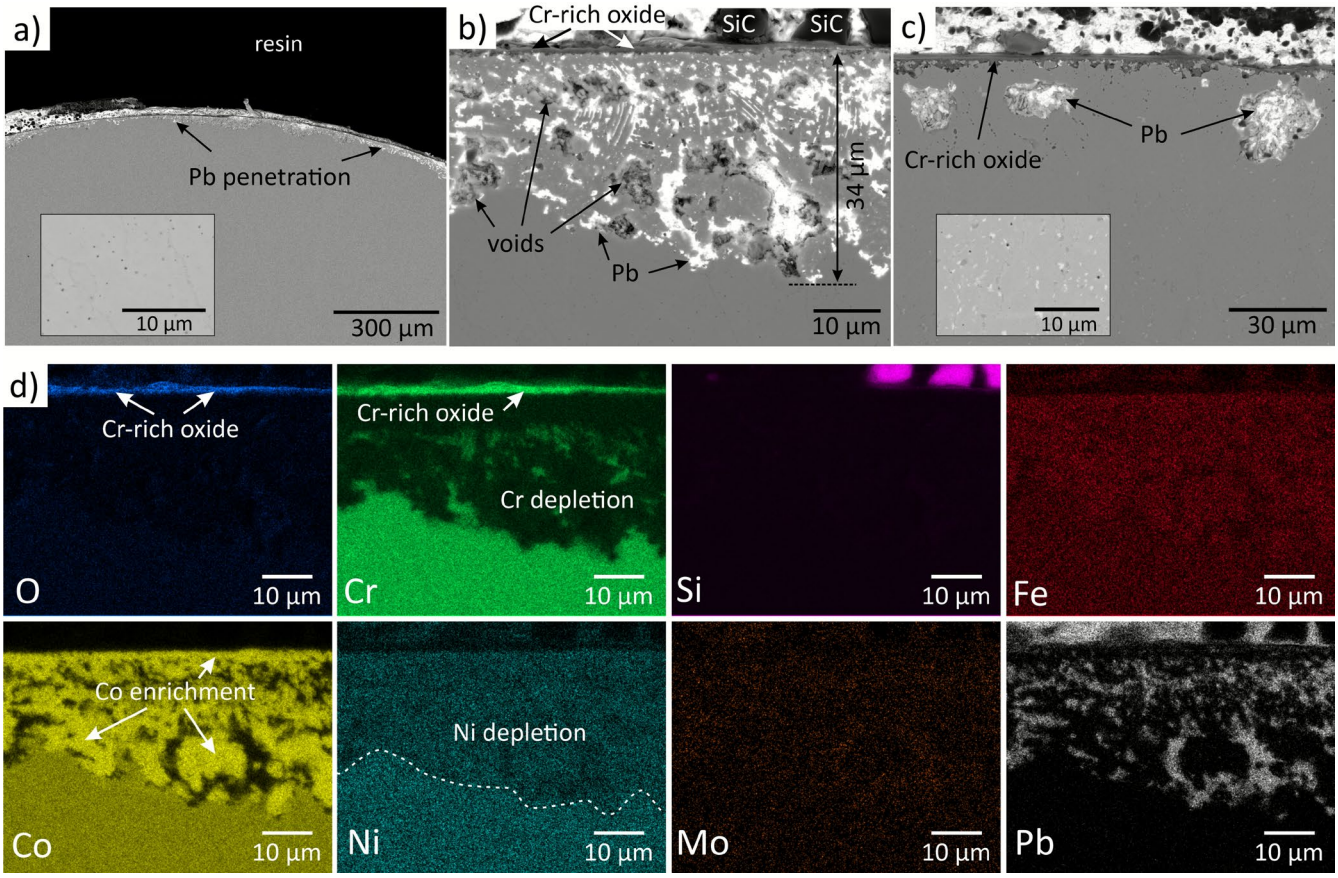

FIGURE 1 | Cross-sections of Stellite 21 samples after 2000 h exposures in liquid Pb. (a) BSE image of sample after exposure at 600°C at low magnification (inset: bulk microstructure), (b) higher-magnification view of sample after exposure at 600°C (the SiC particles were embedded during grinding), (c) BSE image of Stellite 21 after exposure at 700°C (inset: bulk microstructure), (d) EDS elemental mapping of the region shown in (b).

protective scale. Instead, the inward-growing oxides allow dissolution of Cr and Ni into the adjacent liquid Pb and penetration of Pb into the alloy. Nevertheless, these oxides mitigate dissolution of Co and Fe. This is concluded from the remains above the oxide, which are strongly depleted in Co and Fe due to the direct exposure to liquid Pb.

The enlarged view in the inset of Figure 2b reveals a heterogeneous bulk microstructure of Stellite 6, consisting of a bright-appearing Co-rich matrix and darker Cr-rich carbides dispersed in the matrix. The carbides have disappeared in the corrosion-affected region due to Cr depletion. As the carbides are mainly responsible for the high wear resistance of Stellite 6, their disappearance will most likely deteriorate the wear resistance of the material.

The inability of Stellite 6 to form a protective Cr-rich oxide scale might be related to the rather large C content, see Table 1, and the microstructure exhibiting large carbides. Since Cr (and Si) is bound in the carbides, only a reduced amount of Cr (and Si) is freely available in the matrix for oxide scale formation.

At the higher exposure temperature of 700°C, Stellite 6 exhibits no significant corrosion attack (Figure 3a). Instead, a continuous Cr-rich oxide scale (2–4 µm thick) forms on the surface and protects the bulk material from Pb corrosion, see inset to Figure 3a. A very thin Si-rich oxide layer (< 1 µm) is observed beneath the Cr-rich oxide scale, which may contribute to enhanced protection by acting as an additional diffusion barrier, see also Figure 3b and EDS elemental mapping in Figure 3c. One localized area (shown in Figure 3b) was observed exhibiting a notably thicker Cr-rich oxide scale with liquid Pb trapped beneath it. This phenomenon likely results from a localized breakdown of the oxide layer or the development of porous oxides. Both Si-rich and Cr-rich oxides are observed on either side of this zone, indicating that the damage is locally confined. Beneath this zone, evidence of Cr depletion and Cr-carbide disappearance is apparent, suggesting outward diffusion of Cr driven by oxide formation or possibly Cr dissolution in this specific location only.

The much better corrosion resistance of Stellite 6 at 700°C compared with the exposure at 600°C is due to the capability to form a continuous and protective oxide scale at the higher temperature. This might be related with the slightly modified microstructure showing less Cr- (and Si-) carbides at 700°C, see inset to Figure 3a compared with enlarged view in Figure 2b. The Cr-rich carbides could act as Cr reservoir for the formation of a protective Cr-rich oxide scale. Driven by the oxidation of Cr, the surface-near carbides dissolve more easily at the higher temperature, and Cr (and Si) diffusion and oxidation kinetics are also enhanced.

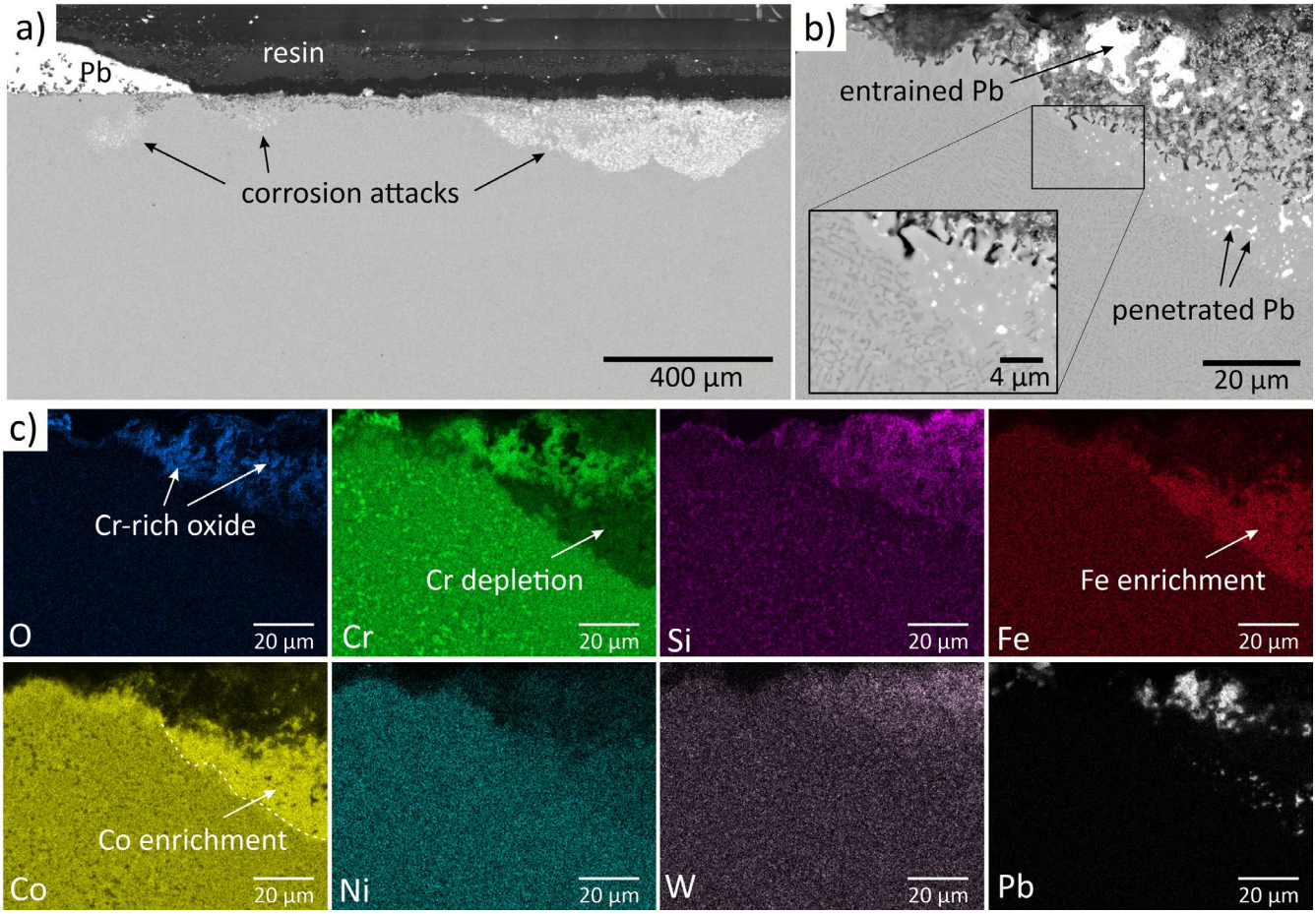

FIGURE 2 | Cross-section of Stellite 6 after 5000 h exposure at 600°C in liquid Pb. (a) BSE image at low magnification, (b) BSE image at higher magnification (inset: zoom to transition region between oxide and bulk), (c) EDS elemental mapping of the region shown in (b).

3.3 | Tungsten Carbide With Co Binder

Figure 4a presents a cross-sectional image of the WC ceramic with Co binder after 5000 h of exposure in liquid Pb at 600°C. The corresponding EDS elemental mapping (Figure 4d) shows depletion of Co in surface-near regions, suggesting that the Co binder has selectively dissolved into the liquid Pb. This is confirmed by the higher-magnification image in Figure 4b, which reveals voids between the WC particles in locations that were originally occupied by the Co binder. The region showing Co binder dissolution and void formation extends up to 18 µm in depth. Assuming a linear time dependence, this result corresponds to a corrosion rate of only 0.03 mm/a. However, the described material degradation can affect the long-term strength of the material, as voids and missing binder between WC grains may cause microcracks under mechanical load or thermal stress. Voids and missing binder can also reduce wear resistance by making it easier for grains to detach, leading to a rougher surface and faster material loss during sliding or abrasion. Cracks and detachment of the outermost bulk material are indeed observed in some locations with Co depletion as indicated in Figure 4a. The detachment runs horizontally through larger areas, suggesting that it was likely caused by thermal shock during the exposure unloading processes or by mechanical stress during preparation of the cross-section sample.

A closer look at the surface of the corroded WC–Co ceramic by EDS elemental mapping (Figure 4d) and BSE surface imaging (Figure 4c) reveals oxide formation on the sample surface and between the WC grains, which is characterized as Cr-rich oxide. Furthermore, XRD analysis of the sample (see Figure 5) indicates the presence of $CrWO_4$ and mixed Cr–Co–Fe-oxides in addition to $CoWO_4$. The formation of the Cr-rich oxides is somewhat unexpected for the WC with Co binder, as Cr is found only in low amounts in the bulk (0.4 wt.% as obtained by EDS measurement). Previous studies have shown that WC–Co cemented ceramics form WO_3 and $CoWO_4$ at 600°C in oxidizing environments [42, 43]. In the present case with low oxygen activity, however, W-oxide and Co–W-oxide are thermodynamically less favored, while the oxidation of Cr and formation of mixed Cr oxides are preferred, as these oxides have lower free energies of formation.

Despite the crack and void formation close to the sample surface, Pb has not penetrated in large amounts into these defects, see EDS elemental mapping (Figure 4d). Most Pb is found adherent to the sample surface, while the Pb signal inside the ceramic is very low and diffuse. The low Pb signal might be explained by inward diffusion of Pb into the ceramic via pre-existing micropores between the Co binder and WC particles during the early stage of exposure. The subsequently formed surface oxides between the WC grains seem

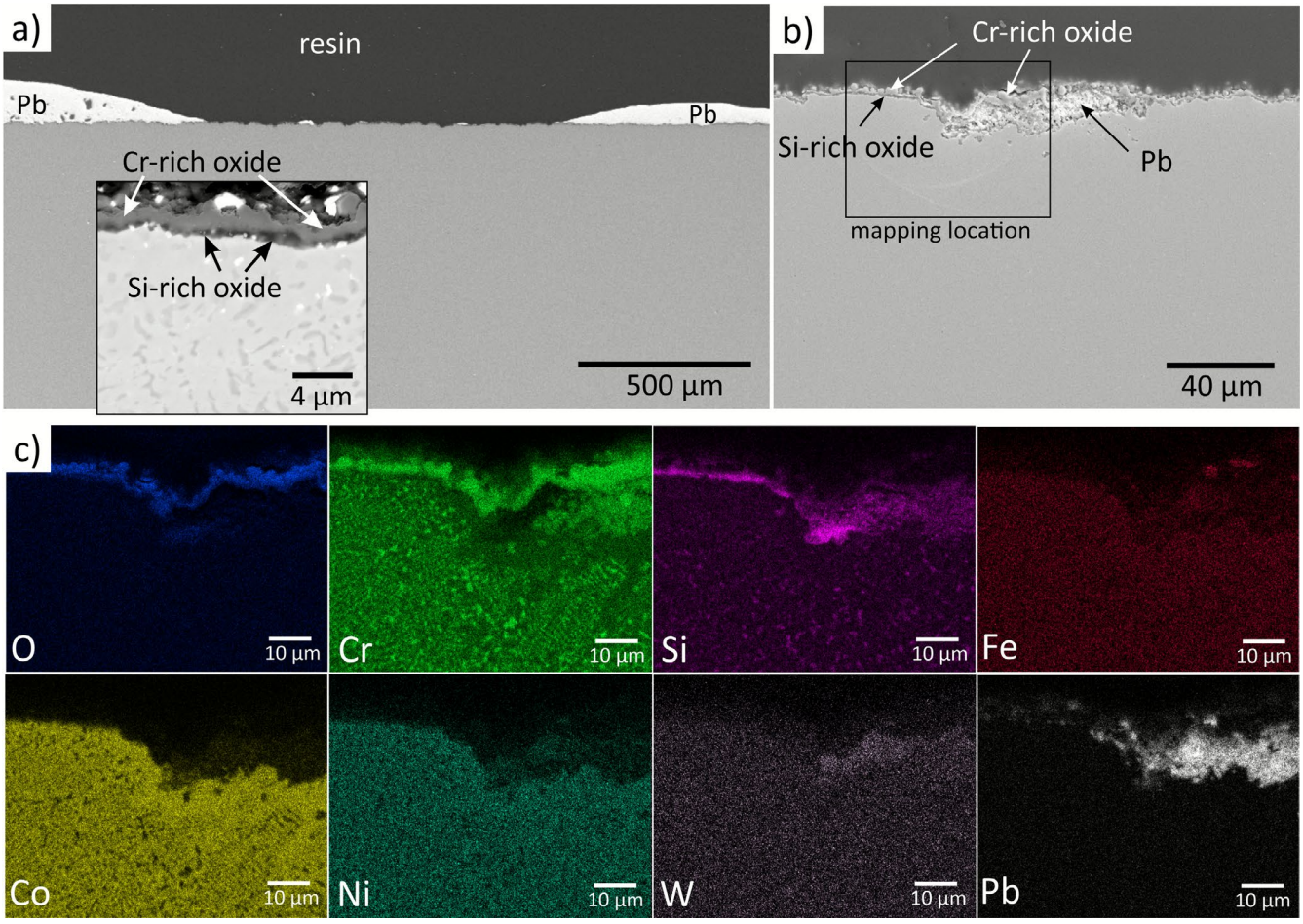

FIGURE 3 | Cross-section of Stellite 6 after 5000 h exposure at 700°C in liquid Pb. (a) BSE image at low magnification (inset shows higher magnification image of typical oxide scale), (b) higher magnification image of a specific region with trapped Pb, (c) corresponding EDS elemental mapping of the region shown in (b).

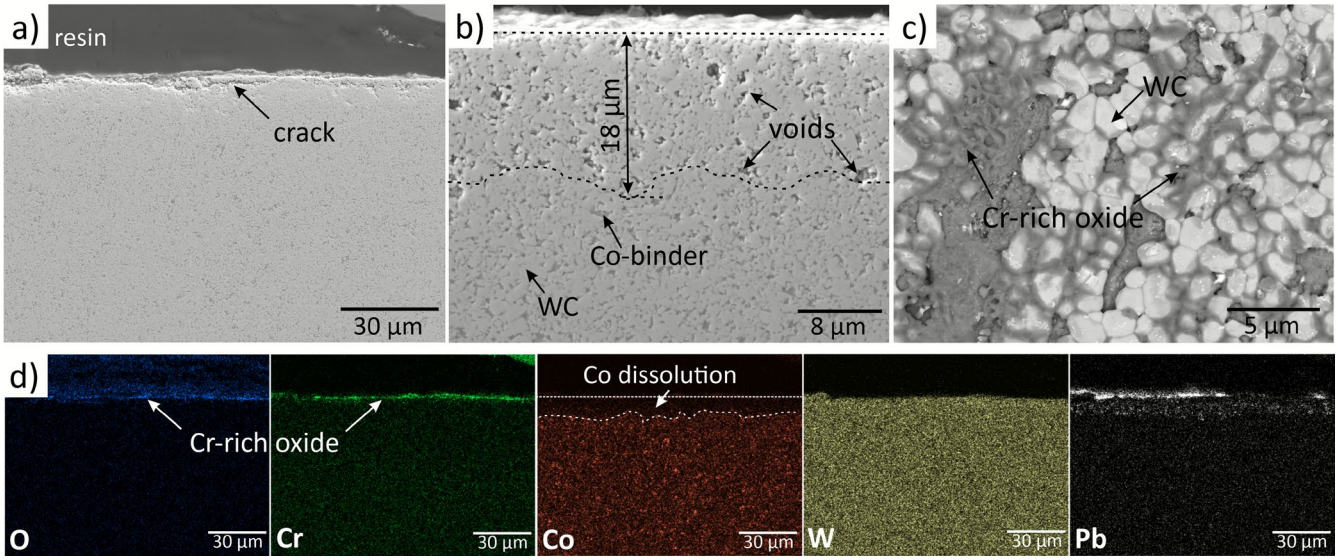

FIGURE 4 | WC–Co ceramic after 5000 h exposure in liquid Pb at 600°C. (a) Cross-section SE image, (b) SE image at higher magnification, (c) surface image showing oxides between the grains, (d) EDS elemental mapping of the region shown in (a).

to prevent further Pb penetration at later stages. Another explanation for the low and diffuse Pb signal in the ceramic material could be impurities during the preparation of the cross-section sample, see also the results for WC with Ni/Cr binder presented below.

3.4 | Tungsten Carbide With Ni/Cr Binder

Figure 6a presents the cross-sectional image of the WC ceramic sample with Ni/Cr binder after 5000 h of exposure in liquid Pb at

700°C. The elemental composition along the red arrow (results shown in Figure 6b) reveals the formation of an oxide scale rich in Cr on the surface of the ceramic. The inner part of the oxide layer is also enriched in W. XRD analysis (Figure 5) confirms the presence of Cr_2O_3 and $CrWO_4$. The binder phase directly below the oxide scale (see Ni enrichment in the line scan) is depleted in Cr due to selective Cr oxidation. In some locations, also Ni is depleted in surface-near regions to variable depths, most probably due to dissolution into the adjacent liquid Pb, leaving behind voids in the material where formerly binder was located. As shown in the higher magnification image in Figure 6c and in the corresponding EDS elemental mapping (Figure 6d), the region with voids due to binder dissolution extends to a depth of approximately 5 μm. This observation suggests that the Cr-rich oxide layer is not uniformly protective across the surface. Potential causes include structural imperfections in the oxide scale, which allow interaction with the underlying binder phase. Similar results are obtained for the 2000 h exposure test of WC with Ni/Cr binder to liquid Pb at 700°C. Here, voids due to binder dissolution reach a depth of 1–2 μm.

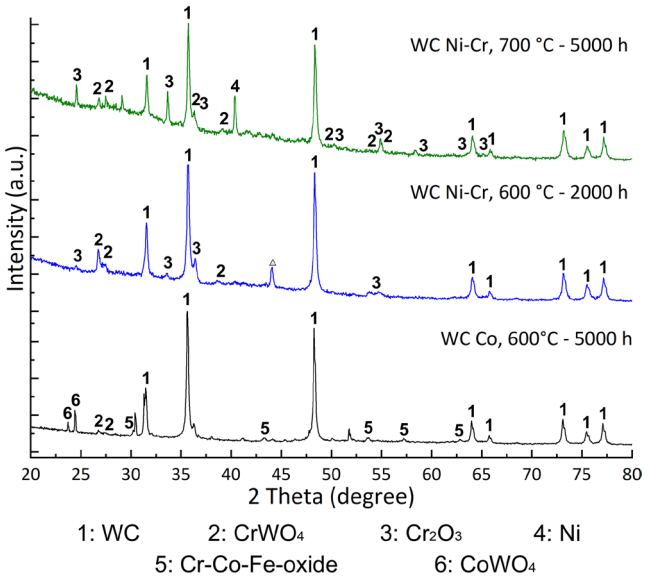

FIGURE 5 | XRD pattern of tungsten carbides after Pb exposures as indicated.

The WC-Ni-Cr-cemented ceramic exposed for 2000 h to liquid Pb at 600°C shows the same corrosion behavior as when exposed at 700°C, though to a lower extent, including the formation of a Cr-rich oxide layer on the surface (see Figure 5) and void formation due to binder dissolution in surface-near regions below the oxide scale. At 600°C, the depth of binder dissolution remains below 1 μm after 2000 h of exposure to liquid Pb.

Although voids are found at both temperatures, liquid Pb penetration into the voids is not observed. Instead, a diffuse low-intensity Pb signal is obtained in regions rather far away from the sample surface, which could stem from Pb impurities during preparation of the cross-section sample. To summarize, WC with Ni/Cr binder shows excellent corrosion resistance when exposed to liquid Pb at 600°C and 700°C, with an estimated corrosion rate below 0.01 mm/a at both temperatures.

4 | Conclusion

The corrosion behavior in liquid Pb of four different materials with high wear resistance was characterized. From the corrosion features observed after 2000 to 5000 h of exposure to molten Pb with 2×10^{-7} wt.% dissolved oxygen at 600°C and 700°C, respectively, the following conclusions are drawn:

- The Cr-rich oxide scale formed on the Co-Cr-based alloy Stellite 21 is not protective and allows significant outward diffusion of alloying elements (mainly Cr). Pb penetrates into the resulting voids. At both temperatures, the corrosion attack reaches a depth of up to 40 μm after 2000 h, which corresponds to a corrosion rate of 0.18 mm/a.
- The corrosion behavior of Stellite 6 strongly depends on temperature. At 600°C, inward-growing oxidation occurs,

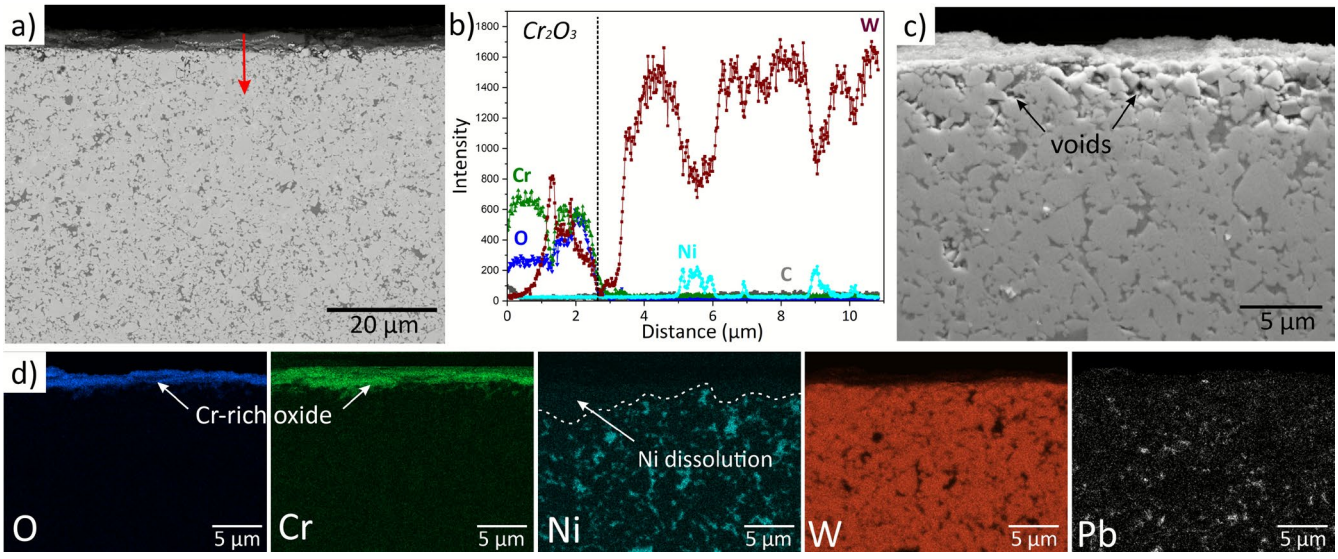

FIGURE 6 | WC ceramic after 5000 h exposures in liquid lead at 700°C. (a) BSE image and location of line scan, (b) corresponding EDS line scan result, (c) SE image with higher magnification, (d) EDS elemental mapping of (c).

which is not protective and results in dissolution corrosion and Pb penetration up to a depth of 200 μm after 5000 h (corrosion rate 0.35 mm/a). In contrast, Stellite 6 shows excellent corrosion resistance at 700°C thanks to the formation of a protective oxide scale composed of an outer Cr-rich layer and an inner Si-rich oxide.

- Despite the formation of a Cr-rich oxide scale, cemented tungsten carbides (WC) exhibit dissolution of the binder material at either exposure temperature, leaving behind voids and an unstable carbide structure in the corroded region.
- The depth of binder dissolution is only 5 μm after 5000 h at 700°C (corrosion rate < 0.01 mm/a at both temperatures) for the WC–Ni–Cr-cemented ceramic, demonstrating very good corrosion resistance. With 18 μm depth of binder dissolution after 5000 h at 600°C, the WC–Co-cemented ceramic shows a slightly higher corrosion rate of 0.03 mm/a.

For a final assessment of the compatibility of the investigated Stellite alloys and WC-based cemented ceramics with liquid Pb, further corrosion tests are recommended, including exposure tests with prolonged duration, at lower temperatures, or subjected to temperature changes, and component tests under real conditions.

Funding

This work was supported by the Bundesministerium für Wirtschaft und Klimaschutz (03EE5050C).

Acknowledgment

Open Access funding enabled and organized by Projekt DEAL.

Conflicts of Interest

The authors declare no conflicts of interest.

Data Availability Statement

The data that support the findings of this study are available from the corresponding author upon reasonable request.

References

1. *Innovation Outlook: Thermal Energy Storage* (International Renewable Energy Agency IRENA, 2020).

2. A. M. Pantaleo, S. Trevisan, F. Matteucci, and L. F. Cabeza, "Innovation Trends on High-Temperature Thermal Energy Storage to Defossilize Energy Systems," *Journal of Energy Storage* 103 (2024): 114261, https://doi.org/10.1016/j.est.2024.114261.

3. A. Heinzel, W. Hering, J. Konys, et al., "Liquid Metals as Efficient High-Temperature Heat-Transport Fluids," *Energy Technology* 5 (2017): 1026–1036, https://doi.org/10.1002/ente.201600721.

4. G. Alva, Y. Lin, and G. Fang, "An Overview of Thermal Energy Storage Systems," *Energy* 144 (2018): 341–378, https://doi.org/10.1016/j.energy.2017.12.037.

5. J. Pacio, C. Singer, T. Wetzel, and R. Uhlig, "Thermodynamic Evaluation of Liquid Metals as Heat Transfer Fluids in Concentrated Solar Power Plants," *Applied Thermal Engineering* 60 (2013): 295–302, https://doi.org/10.1016/j.applthermaleng.2013.07.010.

6. D. Stahl, F. K. Boese, and S. Kostrzewa, "System and Components Design of a Sodium Heat Transfer Circuit for Solar Power Plants," *Electric Power Systems Research* 3 (1980): 151–161, https://doi.org/10.1016/0378-7796(80)90002-4.

7. M. V. Bozorg, J. Coventry, and J. F. Torres, "Thermal Energy Storage in a Tightly Packed Bed With Sodium as the Heat Transfer Fluid: A Numerical Study," *Applied Energy* 352 (2023): 121879, https://doi.org/10.1016/j.apenergy.2023.121879.

8. K. Niedermeier, L. Marocco, J. Flesch, G. Mohan, J. Coventry, and T. Wetzel, "Performance of Molten Sodium vs. Molten Salts in a Packed Bed Thermal Energy Storage," *Applied Thermal Engineering* 141 (2018): 368–377, https://doi.org/10.1016/j.applthermaleng.2018.05.080.

9. K. Niedermeier, "A Perspective on High-Temperature Heat Storage Using Liquid Metal as Heat Transfer Fluid," *Energy Storage* 5 (2023): e530, https://doi.org/10.1002/est2.530.

10. K. Niedermeier, F. Müller-Trefzer, and L. Marocco, "Parametric Study of Filler Size and Properties for a Liquid-Metal Thermal Energy Storage," *Applied Thermal Engineering* 212 (2022): 118568, https://doi.org/10.1016/j.applthermaleng.2022.118568.

11. F. Müller-Trefzer, K. Niedermeier, M. Daubner, and T. Wetzel, "Experimental Investigations on the Design of a Dual-Media Thermal Energy Storage With Liquid Metal," *Applied Thermal Engineering* 213 (2022): 118619, https://doi.org/10.1016/j.applthermaleng.2022.118619.

12. A. Heinzel, A. Weisenburger, and G. Müller, "Corrosion Behavior of Austenitic Steel AISI 316L in Liquid Tin in the Temperature Range Between 280°C and 700°C," *Materials and Corrosion* 68 (2017): 831–837, https://doi.org/10.1002/maco.201609211.

13. T. Emmerich and C. Schroer, "Corrosion in Austenitic Steels and Nickel-Based Alloys Caused by Liquid Tin at High Temperature," *Corrosion Science* 120 (2017): 171–183, https://doi.org/10.1016/j.corsci.2017.02.025.

14. A. Rinaldi, G. Barbieri, E. Kosykh, P. Szakalos, and C. Testani, "Materials for High Temperature Liquid Lead Storage for Concentrated Solar Power (CSP) Air Tower Systems," *Materials* 14 (2021): 3261, https://doi.org/10.3390/ma14123261.

15. H. Glasbrenner, J. Konys, G. Mueller, and A. Rusanov, "Corrosion Investigations of Steels in Flowing Lead at 400°C and 550°C," *Journal of Nuclear Materials* 296 (2001): 237–242, https://doi.org/10.1016/S0022-3115(01)00522-0.

16. Y. Kurata, M. Futakawa, and S. Saito, "Corrosion Behavior of Steels in Liquid Lead–Bismuth With Low Oxygen Concentrations," *Journal of Nuclear Materials* 373 (2008): 164–178, https://doi.org/10.1016/j.jnucmat.2007.05.051.

17. A. Heinzel, A. Weisenburger, and G. Müller, "Corrosion Behavior of Austenitic Steels in Liquid Lead Bismuth Containing 10^{-6} wt% and 10^{-8} wt% Oxygen at 400–500°C," *Journal of Nuclear Materials* 448 (2014): 163–171, https://doi.org/10.1016/j.jnucmat.2014.01.046.

18. K. Lambrinou, V. Koch, G. Coen, J. den Van Bosch, and C. Schroer, "Corrosion Scales on Various Steels After Exposure to Liquid Lead–Bismuth Eutectic," *Journal of Nuclear Materials* 450 (2014): 244–255, https://doi.org/10.1016/j.jnucmat.2013.09.034.

19. A. Weisenburger, C. Schroer, A. Jianu, et al., "Long Term Corrosion on T91 and AISI1 316L Steel in Flowing Lead Alloy and Corrosion Protection Barrier Development: Experiments and Models," *Journal of Nuclear Materials* 415 (2011): 260–269, https://doi.org/10.1016/j.jnucmat.2011.04.028.

20. *Handbook on Lead-Bismuth Eutectic Alloy and Lead Properties, Materials Compatibility, Thermal-Hydraulics and Technologies* (OECD Publishing, 2015).

21. J. Ejenstam and P. Szakálos, "Long Term Corrosion Resistance of Alumina Forming Austenitic Stainless Steels in Liquid Lead," *Journal of Nuclear Materials* 461 (2015): 164–170, https://doi.org/10.1016/j.jnucmat.2015.03.011.

22. K. Lambrinou, E. Charalampopoulou, T. der Van Donck, R. Delville, and D. Schryvers, "Dissolution Corrosion of 316L Austenitic Stainless Steels in Contact With Static Liquid Lead-Bismuth Eutectic (LBE) at 500°C," *Journal of Nuclear Materials* 490 (2017): 9–27, https://doi.org/10.1016/j.jnucmat.2017.04.004.

23. D. Petrescu, F. Golgovici, M. Corban, O. Brincoveanu, and I. Demetrescu, "Effect of Oxygen Concentration on the Corrosion Behaviour of Coated and Uncoated 316L Stainless Steel in Liquid Lead," *Applied Sciences* 15 (2025): 10572, https://doi.org/10.3390/app151910572.

24. G. Müller, A. Heinzel, G. Schumacher, and A. Weisenburger, "Control of Oxygen Concentration in Liquid Lead and Lead–Bismuth," *Journal of Nuclear Materials* 321 (2003): 256–262, https://doi.org/10.1016/S0022-3115(03)00250-2.

25. A. Purwitasari, C. Oskay, A. Heinzel, R. Fetzer, A. Weisenburger, and G. Müller, "Corrosion of Austenitic Stainless Steels in Liquid Pb With $2E^{-7}$ wt% Oxygen at 600 and 700°C," *Corrosion Science* 244 (2025): 112651, https://doi.org/10.1016/j.corsci.2024.112651.

26. A. Purwitasari, R. Fetzer, A. Heinzel, C. Oskay, A. Weisenburger, and G. Müller, "Pb Corrosion of Ferritic/Martensitic Steels at 600–700°C," *Corrosion Science* 255 (2025): 113142, https://doi.org/10.1016/j.corsci.2025.113142.

27. A. Purwitasari, R. Fetzer, A. Heinzel, C. Oskay, A. Weisenburger, and G. Müller, "Influence of Aluminizing and Pre-Oxidation on Corrosion Behavior of 316Ti in Liquid Pb at 600–700°C," *Corrosion Science* 251 (2025): 112896, https://doi.org/10.1016/j.corsci.2025.112896.

28. M. Del Giacco, A. Weisenburger, and G. Mueller, "Fretting Corrosion of Steels for Lead Alloys Cooled ADS," *Journal of Nuclear Materials* 450 (2014): 225–236, https://doi.org/10.1016/j.jnucmat.2013.07.005.

29. H. Chen, Z. Feng, G. Mei, W. Tan, and G. Zhu, "The Role of Lead-Bismuth Eutectic Temperature in Affecting Fretting Corrosion of 316L Stainless Steel," *Wear* 572 (2025): 205997, https://doi.org/10.1016/j.wear.2025.205997.

30. M. J. Schneider and M. S. Chatterjee, "Introduction to Surface Hardening of Steels," in *Steel Heat Treating Fundamentals and Processes, ASM Handbook*, ed. J. L. Dossett and G. E. Totten (ASM International, 2013), 389–398, https://doi.org/10.31399/asm.hb.v04a.a0005771.

31. M. F. Aswad, A. J. Mohammed, and S. R. Faraj, "Induction Surface Hardening: A Review," in *Journal of Physics Conference Series* (IOP, 2021), 12087, https://doi.org/10.1088/1742-6596/1973/1/012087.

32. D. Tandon, H. Li, Z. Pan, D. Yu, and W. Pang, "A Review on Hardfacing, Process Variables, Challenges, and Future Works," *Meta* 13 (2023): 1512, https://doi.org/10.3390/met13091512.

33. M. R. Teodoro, H. B. Pereira, M. D. Manfrinato, et al., "Comparative Study of the Abrasive Wear Resistance of Hardfacing FeCrC, FeCrC + Nb, FeTiCW, and FeMn Coating," *Journal of Tribology* 148 (2025): 031403, https://doi.org/10.1115/1.4070135.

34. K. Niedermeier, M. Lux, A. Purwitasari, et al., "Design of the LIMELIGHT Test Rig for Component Testing for High-Temperature Thermal Energy Storage With Liquid Metals," *Processes* 11 (2023): 2975, https://doi.org/10.3390/pr11102975.

35. S. Bassini, C. Sartorio, A. Antonelli, et al., "Exposure Tests of Different Materials in Liquid Lead for LFRs: Effect of the Dissolved Oxygen on Corrosion," in *TMS 2021 150th Annual Meeting & Exhibition Supplemental Proceedings* (Springer International Publishing, 2021), 626–641, https://doi.org/10.1007/978-3-030-65261-6_57.

36. C. Gumiński, "Solubility of Metals in Liquid Low-Melting Metals/Löslichkeit von Metallen in niederschmelzenden Metallen," *International Journal of Materials Research* 81 (1990): 105–110, https://doi.org/10.1515/ijmr-1990-810206.

37. M. I. Pashechko and K. B. Vasyliv, "Solubility of Metals in Fusible Melts," *Materials Science* 31 (1996): 485–493, https://doi.org/10.1007/BF00559143.

38. M. Takahashi and M. Kondo, "Corrosion Resistance of Ceramics SiC and Si3N4 in Flowing Lead-Bismuth Eutectic," *Progress in Nuclear Energy* 53 (2011): 1061–1065, https://doi.org/10.1016/j.pnucene.2011.04.023.

39. X. Li, X. Zeng, Z. Zhao, et al., "Fast-Flowing LBE Corrosion of the SiC Pump Impeller: Numerical and Experimental Investigations," *International Journal of Applied Ceramic Technology* 20 (2023): 436–450, https://doi.org/10.1111/ijac.14201.

40. Q. Li, Y. Zhang, J. Yang, et al., "The Selective Dissolution Corrosion of Silicon Carbide Grain Boundary in Lead-Bismuth Eutectic: Insights From Experimental and First-Principles Investigations," *Corrosion Science* 255 (2025): 113125, https://doi.org/10.1016/j.corsci.2025.113125.

41. G. Müller, G. Schumacher, and F. Zimmermann, "Investigation on Oxygen Controlled Liquid Lead Corrosion of Surface Treated Steels," *Journal of Nuclear Materials* 278 (2000): 85–95, https://doi.org/10.1016/S0022-3115(99)00211-1.

42. V. B. Voitovich, V. V. Sverdel, R. F. Voitovich, and E. I. Golovko, "Oxidation of WC-Co, WC-Ni and WC-Co-Ni Hard Metals in the Temperature Range 500–800°C," *International Journal of Refractory Metals and Hard Materials* 14 (1996): 289–295, https://doi.org/10.1016/0263-4368(96)00009-1.

43. S. N. Basu and V. K. Sarin, "Oxidation Behavior of WC-Co," *Materials Science and Engineering A* 209 (1996): 206–212, https://doi.org/10.1016/0921-5093(95)10145-4.